atmosphere

MDPI

Article

Vertical Variation in the Near-Surface Wind Field over the Kumtag Desert

Junyao Qiu and Yuanli Xie *

College of Urban and Environmental Sciences, Northwest University, Xi'an 710127, China; 18380756283@163.com
* Correspondence: xieyuanli@126.com

Abstract

Vertical wind variations link surface conditions with the overlying airflow and help characterize aeolian forcing in the Kumtag Desert. Existing field observations describe winds close to the ground, but how the timing of wind-speed peaks and the spatial extent of stronger winds change with height remains unclear. This study examined vertical variations in wind speed and direction from 10 to 200 m above ground in the Kumtag Desert across selected periods and terrain settings. We used the Weather Research and Forecasting (WRF) model driven by the fifth-generation European Centre for Medium-Range Weather Forecasts reanalysis (ERA5). Evaluation against 10 m wind speeds at Mangya and Dunhuang stations guided the selection of four five-day periods, totaling 20 days. Hourly wind speeds and directions were extracted at 20 heights from 10 to 200 m above ground level, at 10 m intervals. Above 10 m, the winds were interpolated from the diagnostic 10 m wind and the native mass-level winds. Regional-mean profiles, spatial distributions and local profiles were compared. Regional-mean wind speed increased from 10 to 150 m in all four periods. The largest increase occurred between 10 and 20 m, with weaker increases between 80 and 150 m. Between 150 and 200 m, speeds remained nearly constant or decreased slightly in spring and autumn but increased slightly in summer and winter. Summer had the highest speeds at every height. Winter ranked lowest at 10 m but second highest at 200 m, where wind speed was 1.443 times its 10 m value. Diurnal peaks shifted from 14:00 to 19:00 Beijing Time (BJT, UTC + 8) at 10 m to nighttime or early morning at 200 m. The diurnal wind-speed amplitude, defined as the range of the 24 h composite, generally increased with height. Strong winds persisted over the southern highlands, while stronger lowland winds became more widespread aloft. The increase in mean wind speed from 10 to 200 m differed among the four local analysis windows. At a given height, the ranking of the four representative periods by mean wind speed varied among windows.

Keywords: Kumtag Desert; near-surface wind field; WRF simulation; vertical variation; spatiotemporal characteristics

Academic Editor: Michael L. Kaplan

Received: 27 October 2026
Revised: 20 November 2026
Accepted: 21 November 2026
Published: 26 November 2026

Copyright: © 2026 by the author. Licensee MDPI, Basel, Switzerland. This article is an open access article distributed under the terms and conditions of the Creative Commons Attribution (CC BY) license.

1. Introduction

Near-surface winds provide the driving force for aeolian activity in deserts. Wind speed is closely related to sediment entrainment and potential sand transport intensity [1,2], while wind direction influences transport pathways and dune morphology. The wind that acts at the surface is part of a deeper flow whose vertical structure changes over

the diurnal cycle. Nighttime radiative cooling can weaken vertical mixing and allow winds above a stable surface layer to accelerate [3]. Studies of Saharan dust have shown that the timing of near-surface wind strengthening and momentum transfer from above affects when and where strong winds occur [4,5]. A surface measurement alone therefore describes only part of the wind environment relevant to aeolian processes.

In the Kumtag Desert, early work linked surface winds to feather-like aeolian landforms and related the development of the sand sea to palaeodrainage, erosion, and deposition [6,7]. Zeng et al. [8] used winds measured at 2 m to characterize the diurnal cycle, prevailing directions, and sand-moving winds. Lü et al. [9] used 2 m winds from two sites to infer potential sand transport directions and relate them to dune orientation. More recently, observations of granule ripples at Sanlongsha documented seasonal changes in bedform morphology and migration [10]. These studies relate the surface wind regime to aeolian activity and landforms. They leave open how the winds above the surface vary with height across the desert.

Measurements at multiple heights have since clarified how wind varies vertically in other drylands. Near-surface observations in the Taklimakan Desert related local profiles to thermal stratification and surface energy exchange [11], and tower measurements resolved wind profiles at two sites from 0.5 to 10 m [12]. Soundings and reanalysis revealed nocturnal wind maxima over the basin [13]. On its southern margin, Doppler lidar and ERA5 helped link a low-level jet and daytime surface heating to the development of a deep convective boundary layer [14]. Measurements from Namib dunes showed that the relationship between local direction and the regional wind changes with boundary-layer depth [15]. At Etosha Pan, observed dust emission varied with the evolution of the boundary layer [16]. These studies resolve vertical structure and its evolution at individual sites and provide a basis for asking how those profiles vary across a desert landscape.

Reanalysis and regional simulations extend this analysis to spatially continuous wind fields [17,18]. Taklimakan studies have used numerical simulations to examine the deep summer boundary layer and its circulation [19], boundary-layer parameterizations and large eddies [20], and the relation between nocturnal jets and dust [21]. Multilevel reanalysis has also been used to investigate jet variability for wind-energy assessment [22]. Finer grids can represent more terrain detail, but station-level wind errors depend on both the grid and the forcing [23,24]. The sampling of a near-surface profile also depends on how winds are interpolated between model levels [25]. For the Kumtag Desert, it remains unclear how the timing and strength of winds at different heights vary jointly across the southern highlands and adjacent lowlands.

Here we ask how regional-mean wind speed and direction change between 10 and 200 m above ground level (AGL), how the timing of peak winds varies with height, and how vertical wind profiles differ between highland and lowland settings. We use hourly ERA5-driven WRF winds on a 3 km grid to compare regional profiles, spatial patterns, and four fixed local windows for 20 days selected across four months. This comparison lets us examine how the area of stronger winds and the relative strength of the four periods change with height. We also compare the directions of stronger winds using a height-dependent wind-speed threshold.

2. Materials and Methods

2.1. Study Design

This study examines vertical variations in the wind field at 10–200 m AGL and their temporal and spatial differences through four components: wind-field simulation and evaluation, extraction at fixed heights, analysis of vertical variations, and application of equivalent wind-speed thresholds (Figure 1). Equivalent wind-speed thresholds are

https://doi.org/10.3390/atmos17121176

height-specific wind speeds that correspond to the same reference friction velocity under a neutral logarithmic wind profile with fixed aerodynamic roughness. The complete wind field, comprising all valid wind samples, is analyzed first. Stronger-wind samples are then examined in a separate equivalent-threshold analysis. The procedure is outlined below.

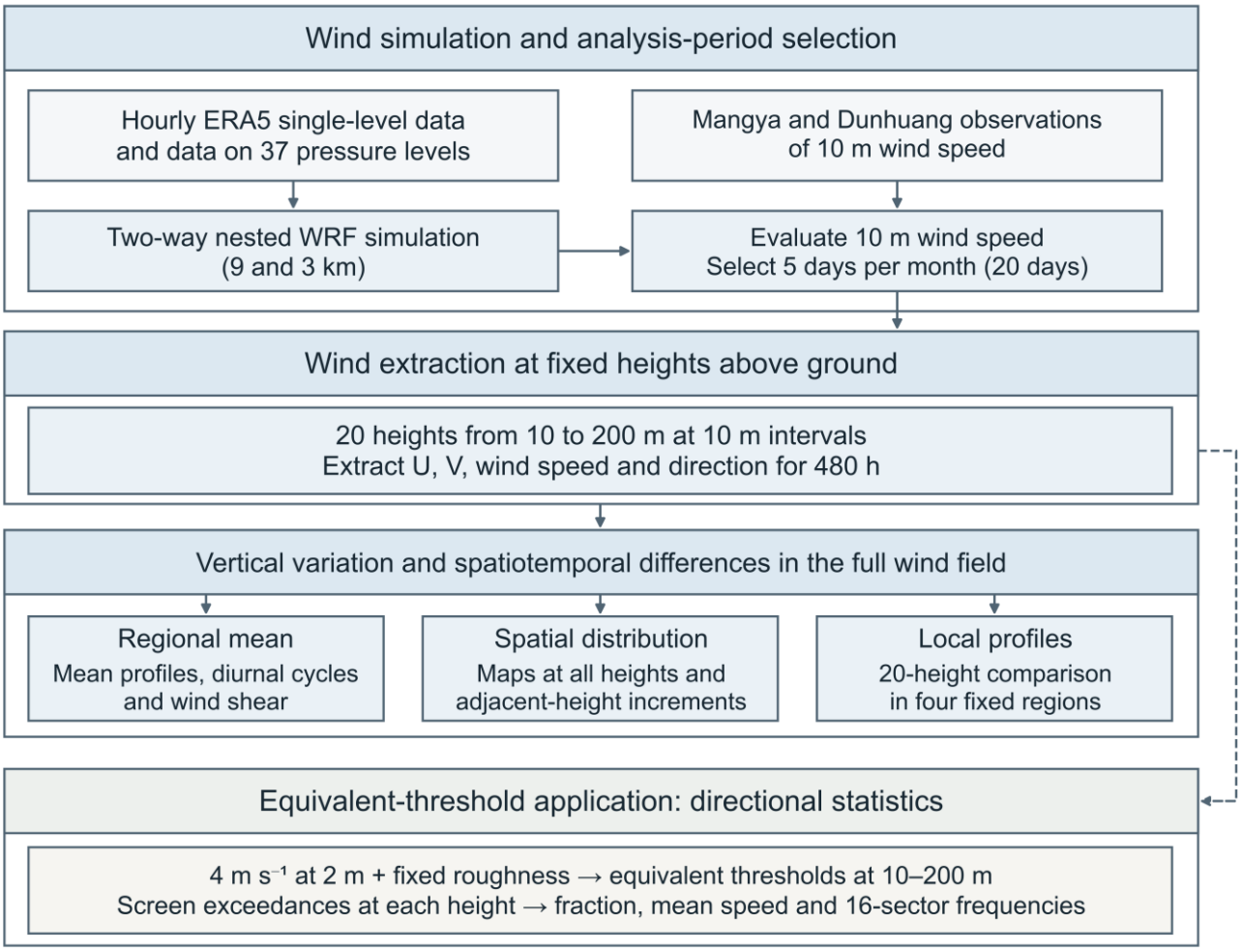


Figure 1. Study workflow. Solid lines indicate wind-field simulation, station-based evaluation, extraction at fixed heights, and analysis of the complete wind field. Dashed lines indicate the separate equivalent-threshold analysis based on the wind fields at fixed heights.

(1) Wind-field simulation and selection of analysis periods. ERA5 data are used to drive WRF to produce hourly wind fields for the four target months. The horizontal grid spacing is 9 km in the outer domain (d01) and 3 km in the inner domain (d02). The simulations use the Asymmetric Convective Model version 2 (ACM2) for the planetary boundary layer (PBL) and the Revised MM5 scheme for the surface layer (Table 1). Simulated 10 m wind speeds are paired with observations at Mangya and Dunhuang for evaluation. Five dates are selected from each month, giving 20 dates for comparison across the four months.

(2) Extraction of wind fields at fixed heights AGL. Twenty heights are defined at 10 m intervals from 10 to 200 m. The model-provided 10 m wind field is retained. Wind fields at 20–200 m are obtained by destaggering the model-level horizontal wind components, rotating them to Earth-relative coordinates, and linearly interpolating between the model-provided 10 m wind and the native mass-level winds, or between two native mass levels. The resulting wind-speed and wind-direction data cover 480 h over the 20 selected dates.

(3) Comparison of vertical variations in the complete wind field. Three aspects are considered: regional characteristics, spatial distributions, and local profiles. Regional analyses examine mean profiles, diurnal wind-speed variations, and vertical wind shear. Spatial analyses compare wind fields at the 20 heights and wind-speed increments between adjacent heights. Local analyses compare profiles in four fixed analysis windows to examine how regional patterns are expressed at different locations.

(4) Analysis of stronger winds. We convert a reference of 4 m s^{-1} at 2 m [8] to a separate threshold at each analysis height, then compare how often that threshold is exceeded and from which directions.

2.2. Study Region and Data

The Kumtag Desert lies southeast of Lop Nur in the Tarim Basin. It borders the Altun Mountains to the south and the Achik Valley to the north, beyond which lie the Beishan Mountains. Its eastern margin grades into the Shule River alluvial–lacustrine plain, and the terrain generally slopes from southwest to northeast [26]. Mobile dunes, Gobi surfaces and lowlands adjoin the southern marginal highlands. Characterizing near-surface winds across these settings helps describe the aerodynamic conditions underlying local aeolian activity. The study region is a rectangle encompassing the Kumtag Desert and its surrounding terrain (89°57′49″–94°54′08″ E, 39°07′50″–41°00′03″ N [8]; Figure 2a,b).

WRF is driven by ERA5 hourly single-level data and data on 37 pressure levels [17], both at 1 h intervals. Observations at Mangya (51886; 38.25° N, 90.85° E) and Dunhuang (52418; 40.15° N, 94.68° E) are used to compare the simulated and observed 10 m wind speeds at those sites and to select analysis dates. The station data are obtained from the NOAA/NCEI Integrated Surface Database [27]. Mangya lies south of the analysis rectangle and Dunhuang lies near its eastern boundary.

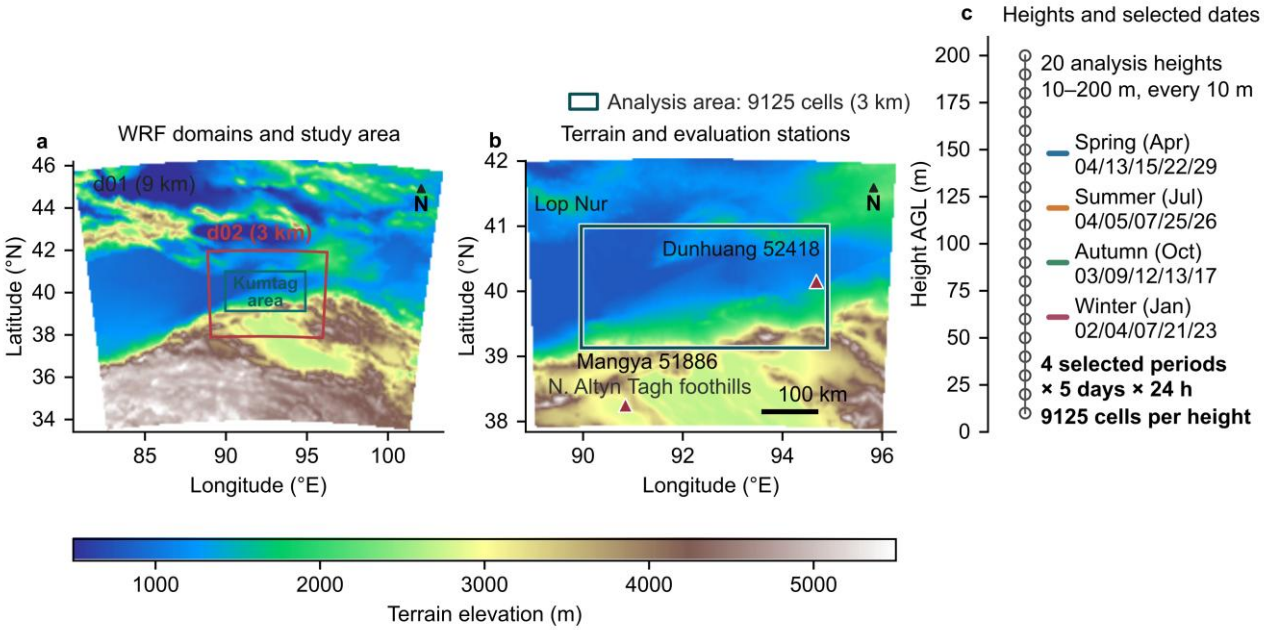


Figure 2. Study region, statistical analysis area, and analysis design. (**a**) Terrain in WRF d01, the d02 boundary, and the location of the Kumtag analysis region. (**b**) Static terrain in d02, the statistical analysis area, and Mangya and Dunhuang stations used for 10 m wind-speed evaluation and date selection. The outline indicates the extent of the 9125 grid cells included in the analysis, with a grid spacing of 3 km. (**c**) The 20 analysis heights and selected dates. Five dates each in April, July, October,

and January form the four case periods, respectively. Calendar dates use Beijing Time (BJT, UTC + 8).

Table 1. WRF-ARW v4.7.1 configuration. Entries spanning the d01 and d02 columns apply to both domains. The 54 s value is the base integration time step specified in the configuration file. It applies to d01. The configured parent-to-nest time-step ratio of 3 gives a nominal time step of 18 s in d02.

Configuration Item	d01 (Outer Domain)	d02 (Inner Domain)
Nesting	Two domains with two-way nesting	
Horizontal grid dimensions	191 × 149	199 × 148
Horizontal grid spacing	9 km	3 km
Vertical grid parameter, e_vert	35 (34 mass levels and 35 w-level interfaces)	
Model-top pressure	50 hPa	
Base integration time step	54 s	
ERA5 forcing update interval	1 h	
Wind-field output interval	1 h	
Planetary boundary-layer scheme	ACM2 [28]	
Surface-layer scheme	Revised MM5	
Land-surface scheme	Noah [29]	
Longwave and shortwave radiation schemes	RRTMG [30]	
Cloud microphysics scheme	WSM6 [31]	
Cumulus parameterization	Kain–Fritsch [32]	Not used

2.3. WRF Configuration and Selection of Analysis Periods

The Advanced Research WRF model (WRF-ARW), version 4.7.1 [18], was configured with two-way nesting between an outer domain (d01) and a finer inner domain (d02). Their horizontal grid spacings are 9 and 3 km, respectively; the model configuration is summarized in Table 1. Wind-field statistics use the 9125 d02 grid cells within the rectangular study region defined above. In this study, grid-cell locations refer to the cell centers to which the wind components are destaggered during post-processing. The grid has 34 mass levels bounded by 35 w levels, the staggered vertical interfaces between adjacent mass layers or at the model boundaries.

The WRF Preprocessing System (WPS), version 4.6.0, used a Lambert conformal grid centered at 40° N, 92° E, with standard parallels of 30° and 60° N. Geogrid interpolated the static terrain and land-cover fields to the model domains, ungrib extracted the ERA5 forcing, and metgrid interpolated that forcing to the model grids before WRF initialization. The model configurations used GMTED2010 terrain and MODIS land-cover data.

Turbulent transport in the atmospheric boundary layer is represented by ACM2. Turbulence refers to irregular fluctuations in airflow. ACM2 represents local turbulent mixing and adds transport between nonadjacent layers by convective eddies under unstable conditions [28]. In the Gurbantunggut Desert, ACM2 reproduced the observed diurnal cycle of 10 m wind speed well [33]. It has also been used in the mesoscale domains of a Taklimakan Desert WRF–large-eddy simulation [20] and in month-long simulations of the Taklimakan Desert [34]. The study uses an established regional model to examine wind structure across periods and terrain settings. We selected ACM2 from its physical formulation and published desert evaluations, and kept the configuration fixed across months. ACM2 has also been selected for long-term wind-resource simulations over Iran following a comparison of boundary-layer schemes [35]. The four simulations began at 08:00 BJT on 31 March, 30 June, 30 September, and 31 December 2022, respectively. At duplicate timestamps after restarts, we retained the first record in source-file name order.

The 1 h ERA5 forcing updates and 1 h output intervals kept the sampling consistent across periods.

Candidate stations are first compared using correlations between observed and simulated 10 m wind speeds over common valid paired times in the four target months. Of the three candidates (Mangya, Dunhuang, and Lenghu), the two highest-ranked stations, Mangya and Dunhuang, are selected and retained throughout. Observed and simulated wind speeds are matched exactly by the Coordinated Universal Time (UTC) timestamp, using only station–time pairs for which both values are valid. We then converted dates and hours for analysis to BJT. Candidate dates extend from the 2nd to the last day of each month and must satisfy all of the following conditions: at least 4 valid pairs per station, at least 12 pairs across the two stations, and a nonnegative daily Pearson correlation coefficient at each station.

Dates were ranked using the Pearson correlation coefficient (R), root-mean-square error (RMSE), and absolute mean bias (|MB|) [36]. Each metric was calculated for the two stations pooled and for the worst-performing individual station for that metric, giving six ranking criteria. The ranks for these six criteria were combined with equal weights, and the five highest-ranked dates were selected from each target month. Using five complete days per month gave each group the same temporal coverage for the diurnal composites and spatial comparisons.

The selected dates are 4, 13, 15, 22, and 29 April 2022; 4, 5, 7, 25, and 26 July 2022; 3, 9, 12, 13, and 17 October 2022; and 2, 4, 7, 21, and 23 January 2023 (Figure 2c). Each five-day group contains 120 h of complete model output. The month and season labels identify the selected analysis periods.

We compared ERA5 and WRF 10 m wind speeds against the same observations at Mangya and Dunhuang. We used all station–time pairs common to ERA5, WRF, and the observations in the four target months. We report the same statistics for the selected dates to describe model agreement in the screened sample. For the spatial comparison, we averaged ERA5 and WRF 10 m scalar wind speeds and horizontal wind components over the same 120 selected hours in each period. The maps retain the native horizontal grids and use the same extent and color scale (Figure S16).

On the 271 paired samples from the selected dates, WRF yielded R = 0.743, RMSE = 2.228 m s^{-1}, and MB = +1.314 m s^{-1} (Table 2; Table S4 gives station-level values). ERA5 yielded R = 0.621, RMSE = 1.953 m s^{-1}, and MB = +0.976 m s^{-1} on the same dates. Across all 1610 common pairs in the four target months, the corresponding statistics were 0.573, 2.620 m s^{-1}, and +1.559 m s^{-1} for WRF, and 0.576, 1.861 m s^{-1}, and +0.929 m s^{-1} for ERA5. ERA5 had lower RMSE and smaller positive bias in both samples. ERA5-driven WRF has been used to examine winds over complex terrain [23] and to assess wind resources over deserts in northwestern China [37].

We used ERA5-driven WRF to examine how 10–200 m wind profiles vary between the southern highlands and adjacent lowlands. The 3 km inner grid represents terrain and land-cover contrasts on a finer horizontal mesh than the 0.25° ERA5 fields used for forcing and comparison. WRF evolves the regional flow under these surface conditions, providing a common three-dimensional field for comparing regional means, spatial patterns and local profiles. In the New European Wind Atlas, ERA5-driven 3 km WRF was used to generate multilevel wind fields [38], depict terrain-related spatial variations [39], and evaluate the added value of downscaling against mast observations [40]. In our matched 10 m maps, WRF depicts a narrow southern strong-wind belt, most pronounced in January, and more local wind-speed variation in July, whereas ERA5 shows smoother distributions (Figure S16). These spatial contrasts provide the context for comparing height-dependent winds between highland and lowland settings. We therefore selected

WRF for the spatially detailed regional wind fields needed to analyze the vertical changes and their spatial differences.

Table 2. Evaluation metrics for 10 m wind speed pooled across Mangya and Dunhuang for the 5 selected dates in each period. N is the number of valid station–time pairs; R is the Pearson correlation coefficient; MB = M − O, where M and O are the mean simulated and observed wind speeds of the paired samples, respectively. Positive MB indicates an overestimate by WRF. RMSE is the root-mean-square error.

Period	N	R	RMSE (m s^{-1})	MB (m s^{-1})
April 2022	75	0.801	2.156	1.141
July 2022	69	0.749	2.248	1.288
October 2022	64	0.551	2.447	1.509
January 2023	63	0.783	2.050	1.349
All 20 days	271	0.743	2.228	1.314

2.4. Extraction of Wind Fields at Fixed Heights from 10 to 200 m Above Ground Level

Twenty fixed heights are defined at 10 m intervals from 10 to 200 m AGL, and all are included in the analysis. Following standard WRF post-processing procedures for the staggered grid and geopotential height [18,41], U10 and V10 are rotated to Earth-relative coordinates to obtain the 10 m wind field. This rotation converts the horizontal wind components from model-grid directions to geographical directions, with the rotated U and V components corresponding to east–west and north–south flows, respectively. WRF-ARW solves the compressible, nonhydrostatic atmospheric equations on its native grid, including the coupled evolution of momentum, mass and thermodynamic variables [18]. The wind responds to advection, pressure-gradient and Coriolis forces, with turbulent transport and surface drag represented by the boundary-layer and surface-layer schemes. We then interpolate the simulated horizontal components to the specified heights above local terrain.

We destaggered the three-dimensional wind components to the mass grid and rotated them to Earth-relative coordinates. The height of each w level was (PH + PHB)/g, where PH and PHB are perturbation and base-state geopotential and g is gravitational acceleration. We averaged the heights of adjacent w levels. We then subtracted the local WRF terrain elevation (HGT) to obtain mass-level heights AGL.

The model-provided 10 m wind field and the mass-level wind fields form the source-height sequence. For each target height from 20 to 200 m, at every grid cell and time, the source levels immediately below and above the target are selected. U and V are linearly interpolated between these levels and then used to calculate wind speed and meteorological wind direction [41], defined as the direction from which the wind comes. We quantified the native sampling and repeated the extraction with linear interpolation in ln(z) rather than z, using identical brackets and endpoint winds. This tests how the choice of an interpolation coordinate affects the derived profiles [25].

HGT is the static terrain elevation from the WRF d02 output. It supplies the terrain backgrounds (e.g., Figure 2b) and the elevation bands (Figure S14). Output files are sorted by filename, and the first record is retained when multiple records share a timestamp. The resulting dataset contains U, V, wind speed, and meteorological wind direction at 20 heights over 480 h and 9125 grid cells. Regional means, daily means, and representative-period composites are calculated from the hourly data across all grid cells. Across 4,380,000 cell–hour profiles, the first mass level ranged from 19.15 to 27.12 m AGL. By month, the median spacing between mass levels 1 and 2 was 51.92–58.67 m, and that between levels 2 and 3 was 66.09–74.47 m. About 99.60% of profiles had three native mass

levels at or below 200 m. The 20 m target lay between 10 m and the first mass level in all April, July, and October profiles and in 99.93% of January profiles. The 30 m target always lay between the first and second mass levels. All 30–40, 40–50, and 50–60 m pairs shared their respective source bracket.

To assess how date selection affected the wind profiles, we also calculated regional means and diurnal composites at 10, 80, 150, and 200 m from all archived hours from the second day through the end of each month. This used 696 h in April and 720 h in each of the other months, for a total of 2856 h. These model-only comparisons used the original height-linear interpolation and required no station filtering.

2.5. Statistics of Vertical Variation and Local Analysis Windows

Vertical wind-field variations are analyzed in terms of regional characteristics, spatial distributions, and local profiles. Regional-mean wind speed is the arithmetic mean of scalar wind speed over valid grid-cell–time samples. Composite wind direction follows climatological statistical practice: U and V are averaged separately and then converted to meteorological wind direction [42]. The wind-speed ratio relative to 10 m is the regional-mean speed at each height divided by the regional-mean speed at 10 m. The directional difference relative to 10 m is the shortest signed rotation from the 10 m resultant direction, positive clockwise (veering) and negative counterclockwise (backing).

For each height in each representative period, wind speeds at the same BJT hour are pooled over all valid grid cells and the 5 dates and then averaged to produce a 24 h composite diurnal curve. Diurnal amplitude is the difference between the maximum and minimum values of this curve. We also calculate the standard deviation of the five daily regional-mean speeds at each height.

Vertical wind shear describes the change in the wind vector with height. Shear between adjacent heights is calculated at each grid cell and time as the magnitude of the wind-vector difference divided by 10 m and then averaged. Bulk wind shear over 10–200 m is the magnitude of the wind-vector difference between 200 and 10 m at the same grid cell and time divided by 190 m, representing the mean vertical rate of wind-vector change between these endpoints. A speed increment is the scalar speed at the upper height minus that at the lower height.

Wind-field maps at the 20 heights across all grid cells are used to identify high- and low-wind-speed areas and changes with height in the extent of stronger winds. Local analysis windows are used to examine how the regional patterns are expressed at specific locations.

Four 3 × 3 grid-cell windows are selected using a common set of rules to compare vertical variations among locations (Table S6). At the d02 grid spacing of 3 km, each window comprises a central grid cell and its 8 surrounding cells. Each window covers approximately 9 km × 9 km when measured along the grid-cell boundaries. The 9 cells are used to calculate the mean wind speed and its minimum–maximum range.

Analysis windows are selected using two metrics calculated from data composited across the four representative periods: mean wind speed across all 20 heights and mean bulk wind shear between 10 and 200 m. R1 is the location with the highest 3 × 3 neighborhood mean wind speed, and R2 is the location with the highest neighborhood mean bulk shear. R3 is the location with the highest neighborhood mean wind speed among grid cells with WRF terrain elevation ≤ 2000 m. R4 is the location where wind speed and bulk shear are closest to their respective medians within the same elevation range. The 2000 m contour separates the southern highlands from the lowland grid cells that account for most of the study region. The centers of R2 and R1, and of R4 and R3, are each separated by at least 12 grid spacings (approximately 36 km, equivalent to 4 window widths) to avoid repeatedly sampling the same high-value patch.

Hourly wind speeds at the 20 heights are calculated in the same fixed analysis windows for all four representative periods. At each height, representative-period mean wind speed is first calculated separately for each of the 9 grid cells. The mean and minimum–maximum range of these 9 means are then calculated to describe spatial differences within the window. Grid-cell-level records are provided in Supplementary Data S1.

Temporal and spatial correlations between heights are calculated using the Pearson correlation coefficient [36] (Figure S12). Temporal correlations use the 120 hourly regional-mean wind speeds in each representative period to measure the coherence of hourly variations across heights. Spatial correlations use representative-period mean wind speeds at the 9125 grid cells to measure the similarity of spatial patterns across heights. Differences among representative periods at the same time of day are summarized by the range of composite wind speeds across the four periods at each BJT hour and height, calculated as the maximum minus the minimum. Comparisons between successive representative periods are calculated as summer minus spring, autumn minus summer, and winter minus autumn. For terrain-stratified statistics, we divide the 9125 grid cells into 8 elevation bands using the WRF static terrain variable HGT. We then summarize mean wind speed at the 20 heights within each band (Figure S14).

To summarize layer-to-layer changes across all 20 heights, mean wind speed is first calculated for each grid cell and selected period. Wind-speed increments are then calculated for the 19 adjacent-height intervals, each spanning 10 m. The median, 25th–75th percentile range, 10th–90th percentile range, and fraction of grid cells with increasing wind speed with height are calculated across the 9125 grid cells for each interval (Figure S15) [36]. Each interval is identified by its upper height; for example, 20 m denotes the 10–20 m interval. Figures S1–S4 show spatial wind fields at the 20 heights, whereas Figure S15 summarizes the distributions of adjacent-height wind-speed increments across all grid cells.

2.6. Equivalent Wind-Speed Thresholds and Directional Statistics

We adopted 4.0 m s^{-1} at 2 m AGL as the reference wind speed. This follows the criterion used by Zeng et al. [8] in Section 2.3 of their Kumtag Desert field study, where they used the relationship between grain size and threshold wind speed to select winds above 4.0 m s^{-1} for their frequency analysis. Field observations at Qira documented different saltation thresholds at different heights, which Shao and Mikami related to friction velocity using a logarithmic profile [43]. Kimura and Shinoda used the same relationship to express threshold friction velocity as a wind speed at 10 m [44]. Laurent et al. [45] applied a neutral logarithmic profile for the same conversion over desert areas of China and Mongolia. We use a spatially uniform reference roughness length of $z_0 = 0.0019$ m from Dunhuang Gobi measurements [46]. A single value gives a consistent sampling criterion across the domain. The conversion assumes a neutral surface layer and zero displacement height [47]. Dividing the wind profile at z by that at 2 m cancels the common threshold friction velocity and gives Equation (1).

$$U_t(z) = 4.0 \times \frac{\ln(z/0.0019)}{\ln(2/0.0019)} \quad (1)$$

Equation (1) gives thresholds of 4.925 and 6.647 m s^{-1} at 10 and 200 m, respectively. All heights share the same reference friction velocity (0.230 m s^{-1} for von Kármán constant 0.40). For example, a 200 m sample enters the wind-direction analysis at that height when the simulated wind speed exceeds 6.647 m s^{-1}. At each height we select speeds strictly greater than the local $U_t(z)$ and divide the number in each of 16 sectors by the total number above that threshold (Tables S1 and S2). Zhang et al. [46] reported a logarithmic mean

roughness length of 0.0019 ± 0.00071 m from intensive observations over the Dunhuang Gobi in May–June 2000, after excluding the influence of buildings. We subtracted and added the reported 0.00071 m to obtain two sensitivity settings, z_0 = 0.00119 and 0.00261 m. We retained 4 m s^{-1} at 2 m and changed only the roughness in Equation (1). The resulting friction velocities are 0.215 and 0.241 m s^{-1}, respectively. The roughness used for this diagnostic is separate from the WRF land-surface parameterization.

2.7. Generative AI Assistance for Translation and Language Editing

The authors used ChatGPT (OpenAI; model: gpt-6.1-sol) to translate author-written Chinese text into English and to edit the English for grammar, clarity, and consistency. The authors reviewed the translation and language edits and take responsibility for the final manuscript.

3. Results

3.1. Overall Vertical Variations in Wind Speed and Direction

Regional-mean wind speed increased from 10 to 150 m in all four periods, with the largest 10 m increment in the 10–20 m interval (0.647–0.763 m s^{-1}). Across 150–200 m, the total change was −0.019 to +0.087 m s^{-1}: speeds decreased slightly in April and October and increased slightly in July and January (Figure 3a,e; Table 3). Table S5 gives the values at all 20 heights.

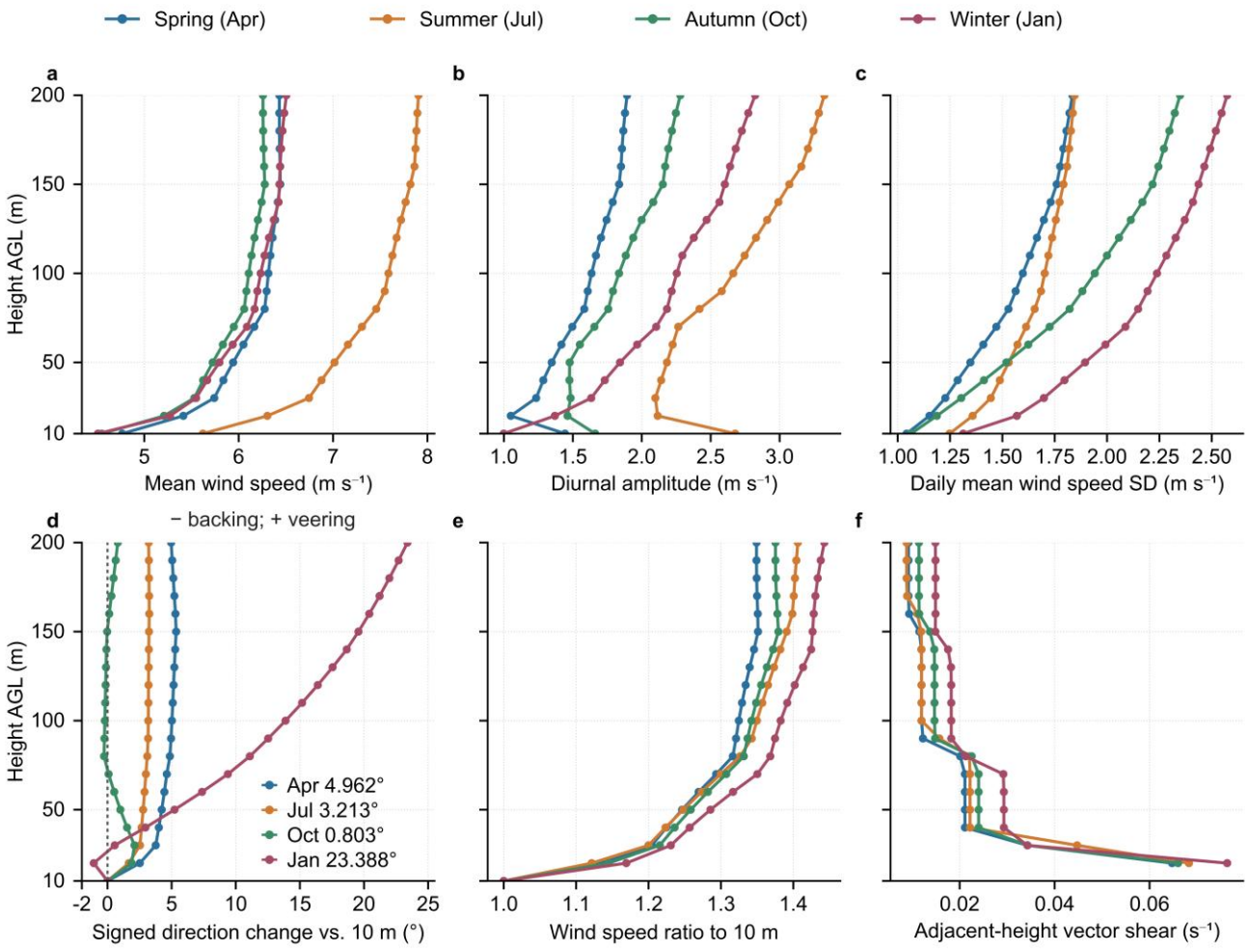


Figure 3. Vertical wind variations at the 20 heights. (**a**) Regional-mean wind speed; (**b**) diurnal amplitude (maximum minus minimum of the 24 h composite curve); (**c**) standard deviation of the

five daily regional-mean wind speeds; (**d**) resultant wind-direction difference relative to 10 m, calculated as the shortest signed angular difference, with positive values indicating clockwise rotation (veering) and negative values indicating counterclockwise rotation (backing). The lower-right legend gives the 200 m minus 10 m directional difference; (**e**) regional-mean wind-speed ratio relative to 10 m; (**f**) vector wind shear between adjacent heights.

The ranking of regional-mean wind speeds among the selected periods changed with height. Summer had the highest mean wind speed at all 20 heights. Winter had the lowest value at 10 m, 4.509 m s^{-1}, but ranked second at 200 m, reaching 6.505 m s^{-1} (Figure 3a). Its wind-speed ratio between 200 and 10 m was 1.443 (Table 3).

The diurnal amplitude of regional-mean wind speed generally increased with height. The standard deviation of the five daily regional means showed the same tendency. Vector wind shear between adjacent heights was strongest within 10–40 m and decreased rapidly aloft (Figure 3b,c,f). The resultant wind-direction differences between 200 and 10 m were approximately 4.962°, 3.213° and 0.803° in spring, summer and autumn, respectively. Winter showed the largest difference, 23.388° (Figure 3d). At 20 m, the winter resultant direction backed relative to 10 m. Replacing linear interpolation in height with linear interpolation in log height changed regional-mean speed by at most 0.121 m s^{-1} across the 80 period–height means. The overall increase to 150 m and the signs of the small 150–200 m changes persisted. The 10–20 m increment increased from 0.647 to 0.763 to 0.721–0.817 m s^{-1} under log-height interpolation.

Table 3. Regional-mean wind speeds (m s^{-1}) at selected heights during the four selected periods. Mean speeds, diurnal peak times and modal directions for all wind samples at all 20 heights are listed in Table S5.

Height (m)	Spring (April)	Summer (July)	Autumn (October)	Winter (January)
10	4.767	5.621	4.550	4.509
20	5.414	6.304	5.210	5.272
80	6.275	7.457	6.059	6.169
150	6.441	7.819	6.276	6.432
200	6.431	7.905	6.258	6.505

3.2. Height-Dependent Changes in the Diurnal Wind-Speed Cycle

The regional-mean wind-speed maximum shifted from afternoon at 10 m to nighttime or early morning at 200 m in all four selected periods (Figure 4a,c,e,g). At 10 m, it occurred between 14:00 and 19:00 BJT. At 200 m, the peaks occurred at 00:00 in April, 22:00 in July, 05:00 in October, and 23:00 in January. These endpoint peak hours persisted under log-height interpolation.

Some intermediate peak hours were sensitive to interpolation. In July, the first height with a 22:00 rather than 20:00 peak moved from 80 to 70 m under log-height interpolation. In October, the first height with a 05:00 rather than 02:00 peak moved from 130 to 120 m. At these heights, the two candidate maxima were close in magnitude.

Using all archived days from the second day of each month, regional-mean wind speeds increased in both the 10–80 and 80–150 m layers in all four months. The increase was larger in the 10–80 m layer (1.357–1.654 m s^{-1}) than in the 80–150 m layer (0.119–0.308 m s^{-1}). The signs of the small 150–200 m changes also persisted.

The timing of minimum regional-mean wind speed and the diurnal amplitude also changed with height. In spring and autumn, minima occurred in the evening near the ground and progressively earlier aloft. In summer, the minimum shifted from 02:00 at 10–20 m to 09:00–10:00 at 30–200 m. In winter, it shifted from 03:00 at 10 m to 15:00 at 120–200 m. Across the selected periods, diurnal amplitude generally increased with height. From

10 to 20 m, amplitude fell from 1.44 to 1.05 m s^{-1} in April, from 2.68 to 2.12 m s^{-1} in July, and from 1.66 to 1.46 m s^{-1} in October. In January, it increased from 1.00 to 1.37 m s^{-1}. The summer amplitude reached 3.324 m s^{-1} at 200 m, while the winter amplitude increased from 0.999 m s^{-1} at 10 m to 2.822 m s^{-1} at 200 m.

Winds were predominantly northeasterly to easterly during the spring, summer and autumn representative periods and westerly during winter. Their exact directions varied with height and time. Figure S6 presents the 16-sector directional frequencies by height for all wind samples.

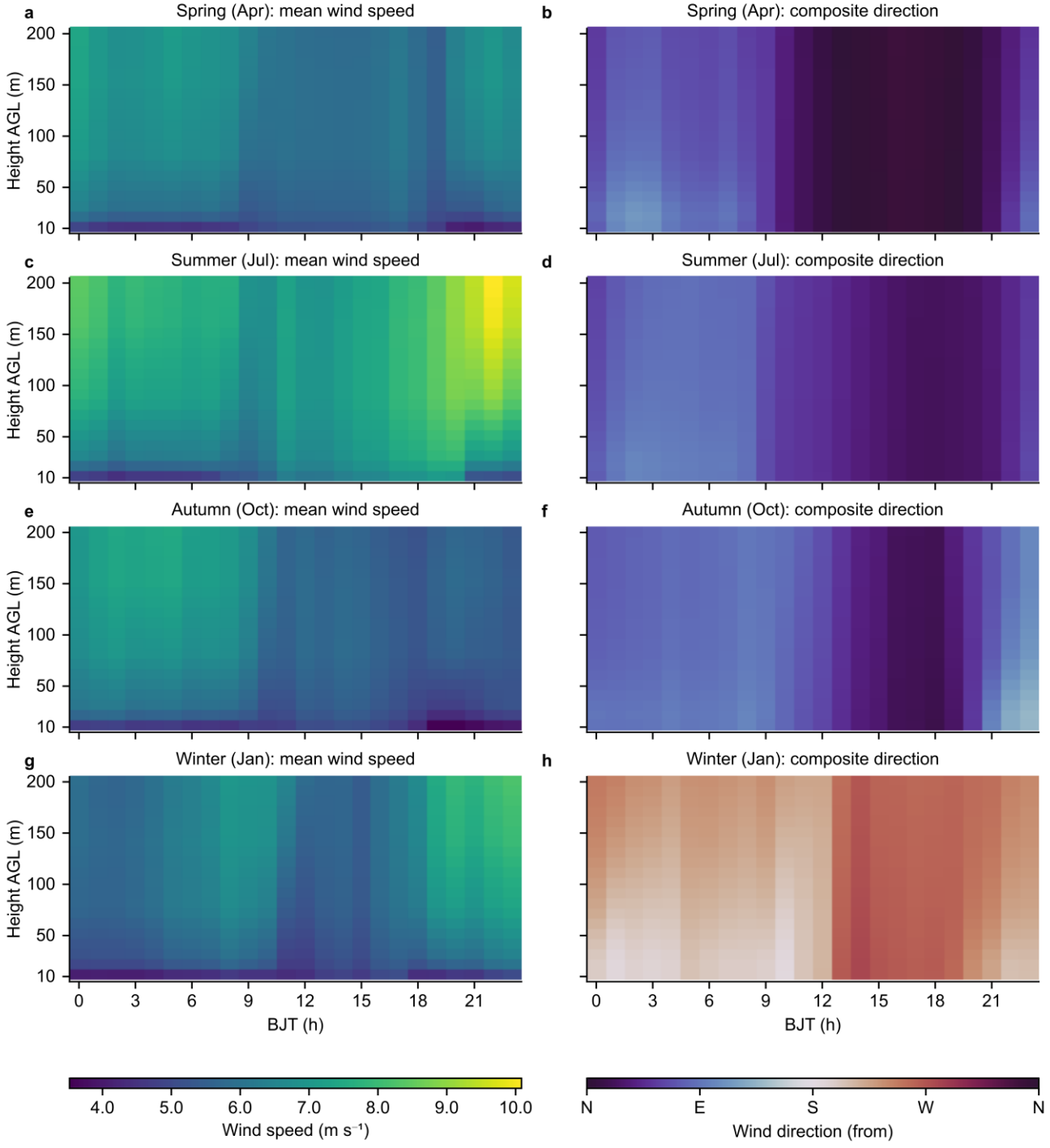


Figure 4. Time–height sections of the wind field during the four selected periods. The left column shows regional-mean wind speed, and the right column shows meteorological wind direction derived from the regional-mean U and V components. Each period comprises five selected dates

and 120 h of wind fields at 9125 grid cells and 20 heights. Each colored cell represents one Beijing Time (BJT) hour and one height, composited from grid-cell values at that hour and height across the five dates. Colors continuously represent the calculated values.

3.3. Changes in the Spatial Wind-Speed Distribution with Height

A strong-wind belt persisted over the southern highlands at all heights, while stronger lowland winds became more widespread aloft (Figure 5). Heights of 10, 100 and 200 m represent the lower, middle and upper parts of the analyzed range in the main text. Figures S1–S4 show all 20 heights at 10 m intervals. Both figure sets retain the spatial distributions across all 9125 grid cells.

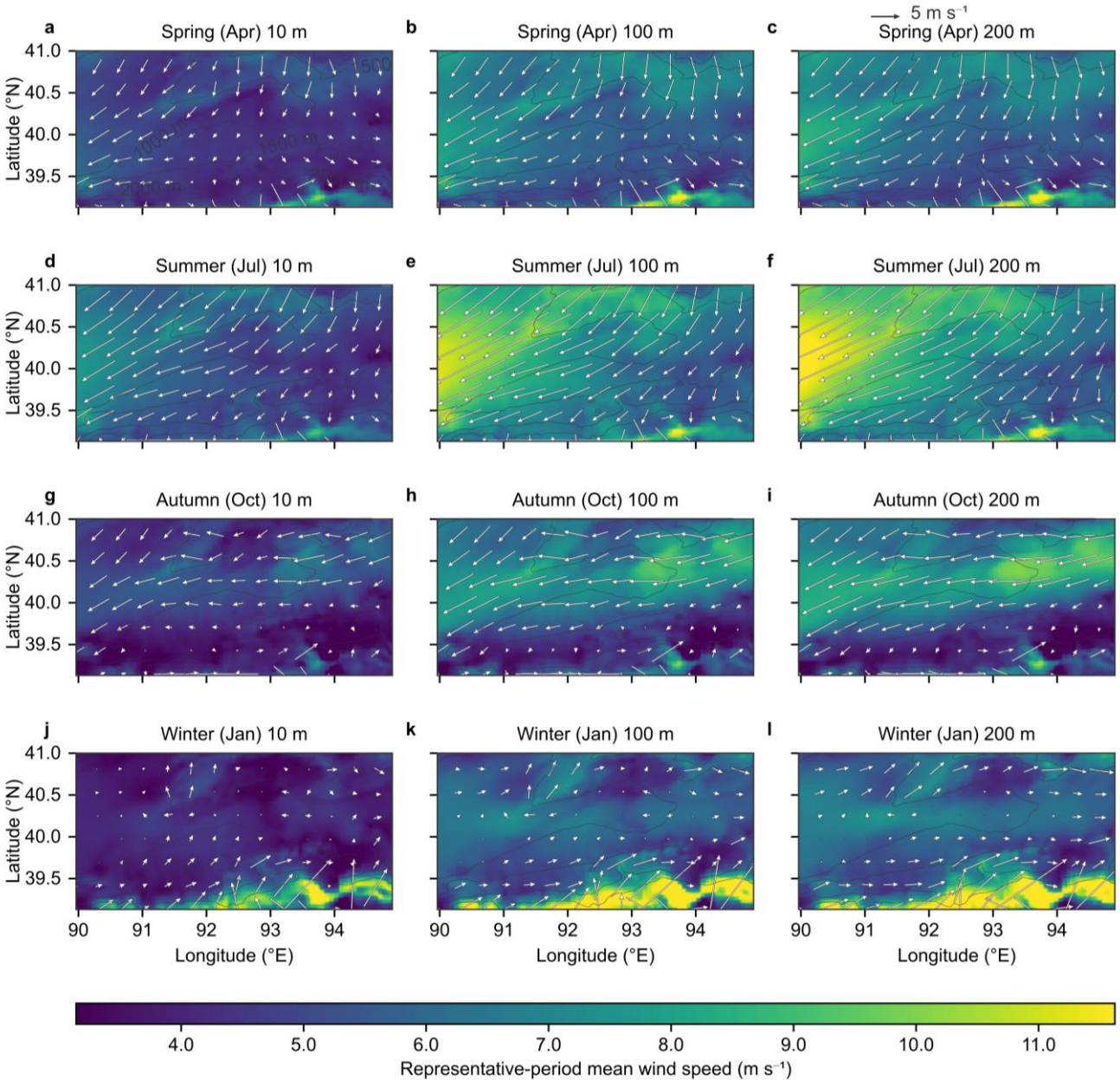


Figure 5. Mean wind speeds and vectors at 10, 100 and 200 m during the four selected periods. White arrows show resultant mean wind vectors; the arrow above the panels represents 5 m s^{-1}. All 12 panels share a continuous color scale. Its limits are the 1st and 99th percentiles of all valid grid-cell wind speeds pooled across those panels. Values outside these bounds use the endpoint colors. Thin contours show WRF terrain elevations of 1000, 1500, 2000 and 2500 m. Elevations are labeled in (**a**), and identical contours are used in the remaining panels. Each panel represents a 120 h

composite for the corresponding period. Colors are extended to the map edges for display; statistics use the 9125 valid grid cells.

In summer, stronger winds covered larger areas of the western and northern lowlands at 200 m than at 100 m, while southern strong-wind patches persisted (Figure 5e,f). Autumn winds were generally weaker at 10 m. Their increases at 100 and 200 m occurred mainly over the central-eastern and northern lowlands, while neighboring high- and low-speed patches persisted along the southern margin. In winter, the strongest 10 m winds were concentrated over the southern highlands. Lowland wind speeds were generally higher at 100 and 200 m than at 10 m.

The period-mean speed increased in both the 10–20 and 20–30 m intervals at all cells (Figure S15). The median of the cell-wise 10–20 m increment ranged from 0.661 to 0.729 m s^{-1} across the periods. Within 80–150 m, the medians for adjacent 10 m intervals were below 0.09 m s^{-1}.

Above 150 m, neighboring areas gained or lost speed with height. Increases predominated in July and January, while April and October had a larger fraction of cells with little change or decreasing speeds. The median increment across any 10 m interval within 150–200 m was between −0.008 and +0.041 m s^{-1}.

3.4. Differences Among Local Wind-Speed Profiles

The four local analysis windows showed different rankings of wind speed among the selected periods (Tables S6–S10). Figure 6a shows the window locations. Figure 6b–e compare profiles from all four windows in April, July, October, and January, respectively. Each window covered approximately 9 km × 9 km. They represented the southern highland high-speed region (R1), southern highland high-shear region (R2), lowland high-speed region (R3), and a lowland location with near-median wind speed and shear (R4). Wind speeds were highest in winter at R1, summer at R3 and autumn at R4. Supplementary Data S1 contains all 2880 grid-cell–height records.

At R1 in the southern highlands, wind speed increased continuously with height at all nine grid cells in all four representative periods. R2 showed greater wind-speed differences among its cells, while its window-mean speed increased with height in all four periods. Both windows showed larger vertical increases in winter (Figure 6e).

At lowland R3, window-mean wind speeds peaked aloft and then decreased slightly towards 200 m.

At R4, window-mean wind speed was highest in autumn, increasing from 5.576 m s^{-1} at 10 m to 8.340 m s^{-1} at 200 m (Figure 6d).

The maps at 20 heights, increments across 19 adjacent-height intervals and local profiles consistently showed spatial differences in vertical wind-speed variation. Temporal correlations between hourly regional-mean wind speeds at 10 and 200 m ranged from 0.679 to 0.906. Spatial correlations between representative-period mean speeds at these heights ranged from 0.855 to 0.951 (Figure S12). Figure S13 shows hourly variations at 10, 100 and 200 m for R1–R4, and Figure S14 summarizes speeds at all 20 heights by WRF terrain elevation. Daily profiles for the five selected dates and across-date standard deviations at each BJT hour are shown in Figures S5 and S7, respectively.

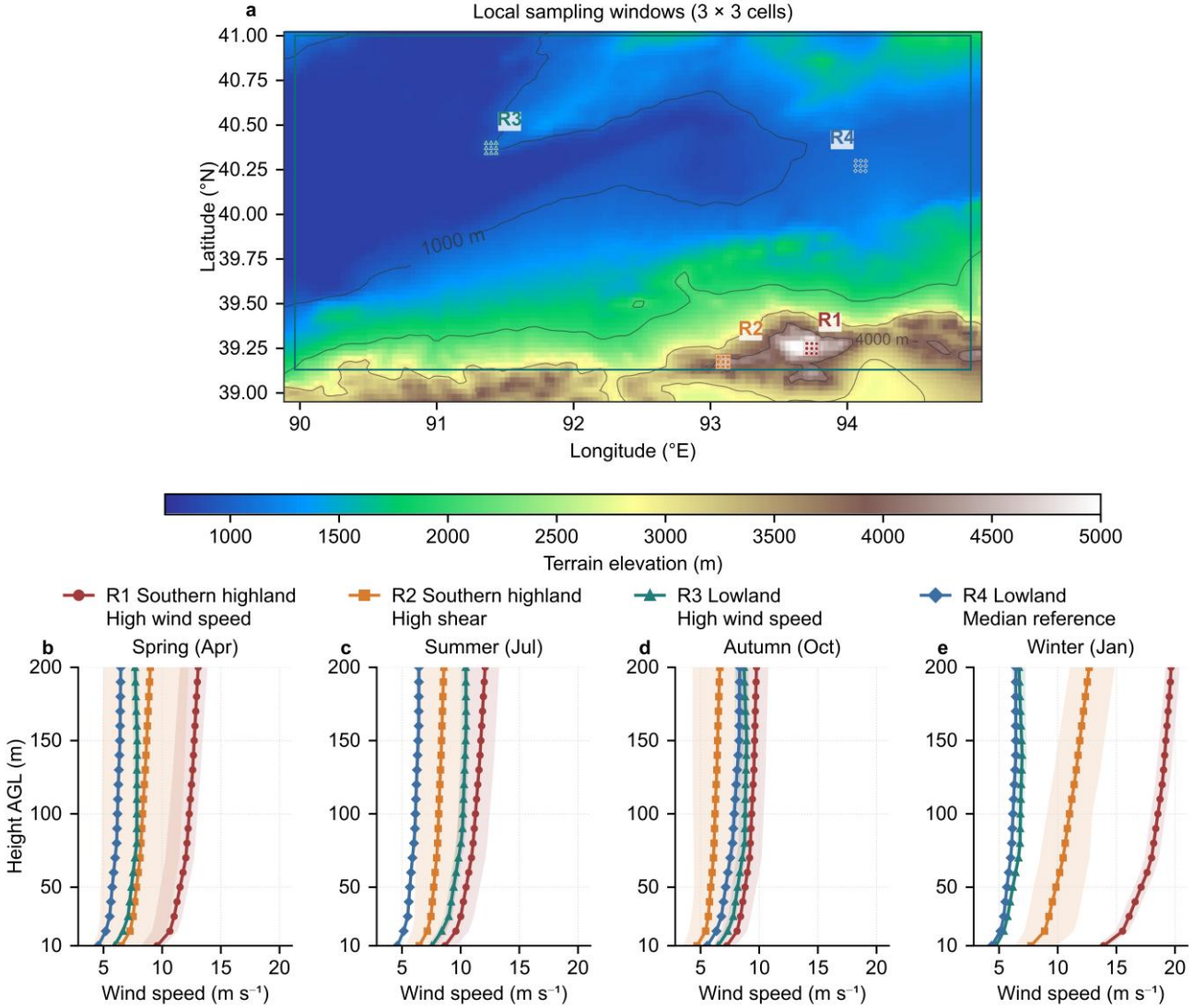


Figure 6. Locations of the local analysis windows and their wind-speed profiles at the 20 heights. (**a**) WRF d02 static terrain, with a turquoise rectangle marking the domain containing the 9125 analyzed grid cells. Colored R1–R4 patches show the boundaries of the 3 × 3 grid-cell windows; small dots mark their nine cell centers. Window centers, coordinate ranges of the grid-cell centers and selection criteria are listed in Table S6. Terrain contours are 1000, 2000, 3000 and 4000 m. (**b**–**e**) Wind-speed profiles from 10 to 200 m during the four selected periods. Solid lines show the nine-cell mean, and shaded bands show the minimum–maximum range of representative-period mean speeds across those cells at each height. The bands describe spatial variation within each window. All profile panels share the same horizontal-axis range, and each window retains a consistent color.

3.5. Wind-Direction Distributions Above the Equivalent Threshold Wind Speeds

Among samples exceeding the equivalent threshold wind speed, modal wind directions varied with height and selected period (Figure 7a–d; Table S2). In spring, east-northeasterly (ENE) winds predominated at 10–170 m, and easterly (E) winds at 180–200 m. In summer, northeasterly (NE) winds predominated at 10–70 m and ENE winds at 80–200 m. At 80 m, the ENE and NE frequencies differed by only 0.016 percentage points. In autumn, ENE winds predominated at 10–60 m and E winds at 70–200 m. In winter, west-southwesterly (WSW) winds predominated at 10–120 m and westerly (W) winds at 130–200 m. At 120 m, WSW and W frequencies differed by only 0.068 percentage points. The nearly equal frequencies of neighboring sectors at 80 m in summer and 120 m in winter

require modal-direction changes to be interpreted alongside frequency differences. At 200 m, the autumn and winter modal directions were E and W, with frequencies of 33.916% and 28.253%, respectively.

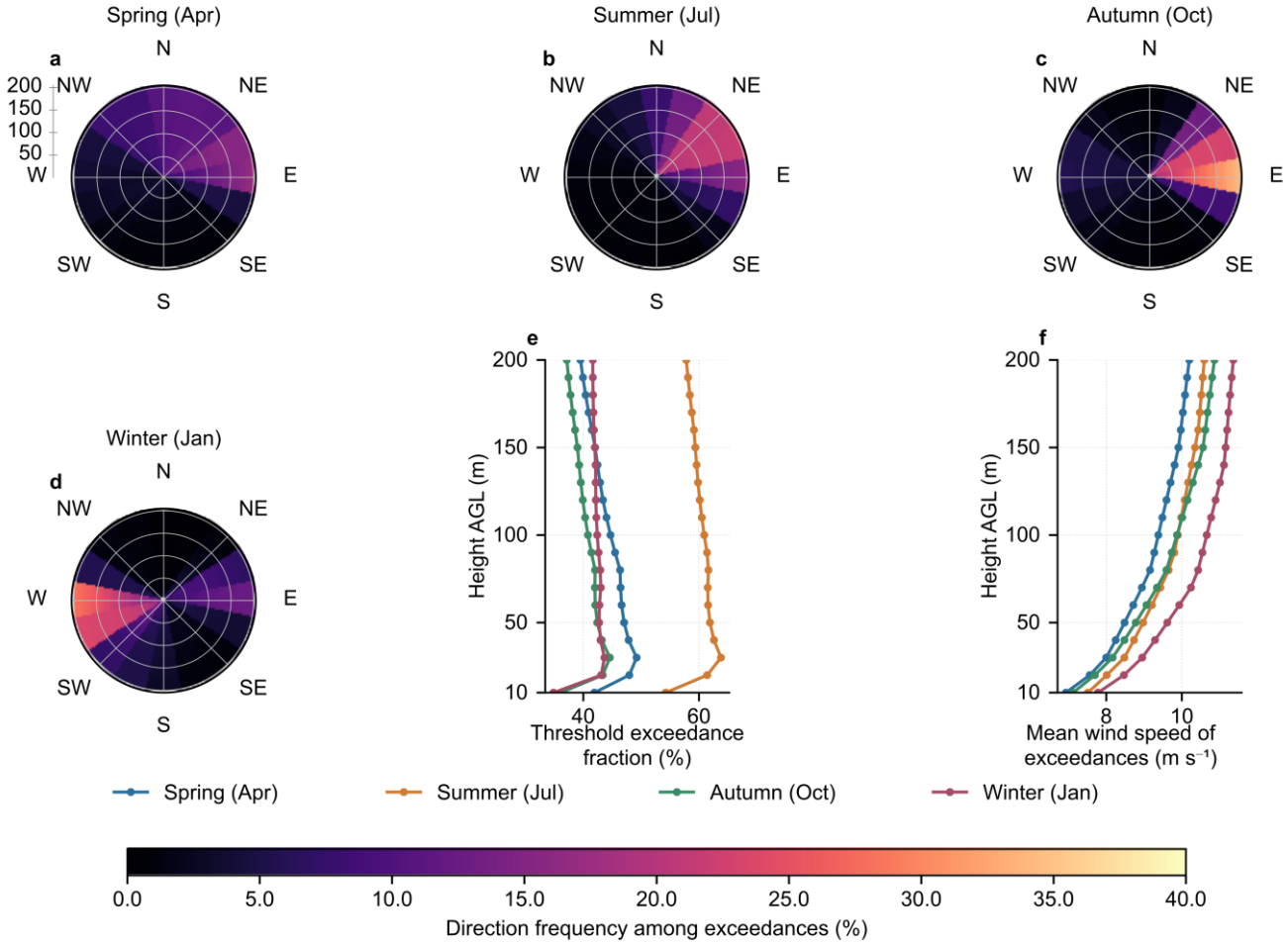


Figure 7. Height-dependent wind-direction distributions for samples exceeding the equivalent threshold wind speed. (**a**–**d**) Frequencies in 16 direction sectors for samples with wind speed strictly greater than $U_t(z)$ at each height. Frequencies are normalized by the total number of above-threshold samples at that height and sum to 100%. Radius denotes height above ground level (m), and the shared continuous color scale spans 0–40%. (**e**) Proportion of above-threshold samples among all valid samples; (**f**) mean speed of above-threshold samples. Height-specific thresholds are derived from a reference of 4 m s^{-1} at 2 m using a neutral logarithmic wind profile with fixed z_0 = 0.0019 m. Each representative period contains 1,095,000 valid samples at each height.

Above-threshold samples accounted for 34.859–63.801% of valid samples across all representative periods and heights. Their proportion peaked at 30 m in every period and generally decreased aloft. Mean speed among these samples increased with height (Figure 7e,f; Tables S1 and S2). Figures S8–S11 present wind roses for all 80 height–period combinations, with each direction sector spanning 22.5°. In spring and autumn, the E-sector frequency among above-threshold samples generally increased with height. It rose from 7.663% and 20.640% at 10 m to 16.707% and 33.916% at 200 m, respectively. NE and ENE frequencies were similar aloft in summer, whereas the W-sector frequency increased with height in winter. Relative to the baseline, the lower roughness increased fractions by 0.83–1.73 percentage points, while the higher roughness decreased them by 0.63–1.31 points. At the lower roughness, the modal sector was unchanged in all 80 period–height combinations. At the higher roughness, it was unchanged in 79 of 80. At 80 m in July, it

shifted from ENE to NE in the higher-roughness case, moving the first ENE level from 80 to 90 m. For this July case (80 m), ENE and NE accounted for 20.937% and 20.920% of above-threshold winds, respectively, at the baseline roughness. At the higher roughness, ENE and NE accounted for 20.994% and 21.071%, respectively, and the above-threshold count fell from 674,929 to 662,902 out of 1,095,000 samples. Supplementary Data S3 reports all three roughness settings for each of the 80 period–height combinations.

4. Discussion

4.1. Relationship to Previous Studies of Vertical Wind Structure

Measurements at 2 m have characterized the Kumtag surface wind regime and related potential sand transport to dune orientation [8,9]. Tower observations at two Taklimakan sites resolved local wind-speed profiles between 0.5 and 10 m [12]. In the Kumtag Desert, combining simulated regional profiles and wind maps over 10–200 m shows how vertical wind changes vary across the selected periods and terrain settings. In the four selected five-day periods, January had the lowest regional mean at 10 m but the second highest at 200 m. The maps show a strong-wind belt over the southern highlands at all analyzed heights and an expansion of stronger winds over the lowlands with height.

Mean wind speed increased from the first to the third native mass level in all four selected periods. Wind speed increased more between the first and second levels than between the second and third. Linear interpolation in height and in log height both showed an overall increase in regional-mean wind speed from 10 to 150 m and smaller changes from 150 to 200 m.

4.2. Height-Dependent Differences in the Diurnal Wind-Speed Cycle

The afternoon peak at 10 m and the later peak at 200 m in the selected periods (Figure 4) can be interpreted in light of changes in vertical mixing over the daily cycle. During daytime heating, turbulent mixing can transfer momentum from faster air aloft toward the surface [14,19]. After sunset, weaker mixing can reduce the effect of surface drag on the flow aloft [3,13,21]. For each of the four periods, we grouped grid-cell–hour samples by the WRF surface sensible heat flux, with positive values indicating heat transfer to the atmosphere. To set aside weak heat exchange, we compared values below −10 W m^{-2} (surface cooling) with those above +10 W m^{-2} (surface heating). The mean 200–10 m wind-speed difference was larger in the cooling group in all four periods (3.01–4.25 m s^{-1} for cooling and 0.77–1.14 m s^{-1} for heating). This association is consistent with weaker vertical coupling during surface cooling. The surface heat-flux groups characterize heating and cooling at the ground. Nocturnal jets can also alter shear and near-surface turbulence [21,48].

The simulated diurnal contrast is also influenced by the representation of turbulent mixing. ACM2 combines local eddy diffusion with nonlocal convective transport under unstable conditions and uses local eddy diffusion under stable conditions [28]. These treatments affect the vertical exchange of momentum and heat and can influence wind-profile shape and the daytime-to-nighttime change in vertical wind-speed differences. Desert and arid-region scheme comparisons show differences in near-surface wind cycles and seasonal performance [33,35]. They provide a physical basis for considering boundary-layer scheme choice when interpreting the height-dependent cycle shown here.

We searched for jet-like profiles on the native grid within 200 m. A candidate core below 200 m had to be faster than both adjacent native mass levels. It also had to exceed the minimum sampled speed on each side within 200 m by at least 2 m s^{-1} and 25%, following the amplitude criterion of Tuononen et al. [49]. Candidates comprised 0.11%, 0.11%, 0.29%, and 0.33% of cell–hour profiles in April, July, October, and January,

respectively. For example, at 00:00 BJT on 4 April near 90.86° E, 39.95° N, the speed at 81 m was 10.75 m s^{-1}, compared with 8.56 and 8.25 m s^{-1} near 25 and 154 m. This screen identifies candidate profiles at individual grid cells and hours.

4.3. Linking Vertical Variations with Spatial Wind Patterns

Exposure to the background flow can favor stronger winds over elevated terrain, and broad slopes can redirect winds toward adjacent lowlands [23,24]. For example, observations along the southern Taklimakan margin identified downslope flow associated with a low-level wind maximum [14]. In the Kumtag simulations, these processes offer possible explanations for the contrast between the southern strong-wind belt and the wider extent of stronger lowland winds aloft (Figures 5 and 6). The southern wind belt resolved in the 10 m WRF maps, particularly in January, adds spatial context to this highland–lowland contrast (Figure S16).

Evaluations elsewhere show that pointwise wind-speed errors do not necessarily decrease following downscaling, partly because finer-scale features are sensitive to timing and location errors [50]. The relative performance of ERA5 and downscaled winds also varies with terrain, height and evaluation metric [51]. In this study, the native-grid map comparison (Figure S16) describes the spatial information supplied by WRF, alongside the paired station statistics reported in Section 2.3.

Near the surface of individual dunes, the wind can depart from the regional direction as a function of dune orientation and boundary-layer depth [15,52]. Our windows span several kilometers and describe their background flow.

4.4. Physical Meaning of the Equivalent Thresholds

The equivalent thresholds provide a common way to sample stronger winds at each height. With the 2 m reference speed held fixed, a larger roughness increases the inferred reference friction velocity. It also raises the equivalent wind-speed thresholds calculated with Equation (1). The broad directional pattern persisted under both tested settings. July at 80 m shows where the inference is more sensitive: the two leading sectors had nearly equal frequencies, so raising the threshold changed their order. The neutral log law applies in the surface layer under the assumptions described in Section 2.6 [47]. Surface roughness varies across dunes and Gobi surfaces [52,53]. Wind profiles above the surface layer can depart from surface-layer similarity [54]. At 200 m, the equivalent threshold is used to select stronger winds aloft for directional analysis. Its physical reference is the speed at that height in the common neutral profile. Actual surface entrainment depends on local surface stress, sediment properties, moisture, and crusts [2,55,56].

4.5. Scope and Limitations

The 20 dates represent selected cases in four months. The same 10 m records were used to screen dates and assess the selected subset, so agreement on those dates describes the screened sample. The longer model series provides a separate check on time sampling. It supports the broad profile changes at the four tested heights. Exact peak hours, the change in diurnal amplitude with height, and the ranking at 200 m depend on the dates included. In the longer samples, the 200 m peaks occurred from evening to morning. The 200 m diurnal amplitude was larger than at 10 m in July and January and slightly smaller in April and October. January ranked below April at 200 m in those samples. Matched observations cover 10 m wind speeds at Mangya and Dunhuang near the study area. Sparse monitoring and limited field resources left the desert interior and southern highlands without matched observations. No concurrent wind profiles were available to validate wind speed, direction, or shear at 20–200 m during the study periods. Paired observations at the corresponding heights would allow us to quantify errors in simulated

layer differences. The positive 10 m bias and larger RMSE than ERA5 in paired comparisons warrant particular caution about small modeled layer differences.

We used one PBL scheme and one vertical grid to examine wind structure with a common model configuration across months. Boundary-layer parameterization can affect simulated winds over complex terrain [57]. A controlled scheme comparison is needed to quantify how ACM2 affects the nighttime wind profile and adjacent-height wind-speed differences in these cases. The literature-based discussion in Section 4.2 identifies the mixing processes through which scheme choice can affect these results. The interpolation test assesses profile reconstruction within this configuration. The 10 m target spacing describes the analysis sampling; the native spacing controls the vertical information available. Small differences between adjacent 10 m targets are more sensitive to reconstruction within a native interval. Where the actual profile curves sharply or has a local maximum between the source levels, interpolation from those levels can miss that feature [25]. The roughness test spans two settings based on one published estimate from the Dunhuang Gobi. The heat-flux groups describe modeled surface heating and cooling. The 200–10 m wind-speed difference alone does not establish the stability of the full layer or whether winds at both heights strengthen at the same time. The upper analysis heights may lie above the local surface layer [54]. Spatially varying roughness and a stability-dependent conversion remain outside the scope of the sensitivity results. A stability-dependent conversion would require stability diagnostics and an estimate of local surface-layer depth to select a wind-profile relation appropriate to the heights being compared. The jet screening covers individual grid cells and hours below 200 m, leaving jet persistence and higher jet cores unresolved. The diagnostics do not separate contributions from jets, synoptic pressure gradients, and terrain-driven flow to the regional peak timing. Diagnosing an internal boundary layer would require a transect under comparable inflow to separate surface transitions from elevation effects. The WRF configuration does not represent feedback from moving sand on the wind. Multi-height observations in the interior and over the southern highlands, together with a boundary-layer scheme comparison, would test the robustness of these case results.

5. Conclusions

(1) Regional-mean wind speed increased from 10 to 150 m in all four selected periods. The largest 10 m increment occurred between 10 and 20 m (0.647–0.763 m s^{-1}). The total change from 150 to 200 m ranged from −0.019 to +0.087 m s^{-1}. In the five-day samples, January ranked lowest at 10 m and second highest at 200 m.

(2) The regional-mean wind-speed peak in the diurnal composites occurred at 14:00–19:00 BJT at 10 m and between 22:00 and 05:00 the next morning at 200 m.

(3) A strong-wind belt persisted over the southern highlands at all 20 analysis heights. In the lowlands, stronger winds became more widespread with height.

(4) In January, the regional resultant wind direction differed by about 23.4° between 10 and 200 m, the largest difference among the four selected periods. In the stronger-wind subset, modal directions above the equivalent thresholds changed with height. Relative to the baseline, the modal direction was unchanged in 80 of 80 combinations at lower roughness and 79 of 80 at higher roughness.

These findings describe four selected five-day periods, one in each target month. The observation-based evaluation covers 10 m wind speeds at Mangya and Dunhuang (Section 4.5). Concurrent wind-profile observations over longer periods would help test whether these patterns persist and directly evaluate the simulated winds and shear at 20–200 m.

Supplementary Materials: The following supporting information can be downloaded at: https://www.mdpi.com/article/10.3390/atmos17121176/s1, Online Resource 1 contains Supplementary Information with Figures S1–S16 and Tables S1–S10. Online Resource 2 contains Supplementary Data S1 (2880 local grid-cell–height records) and S2 (76 adjacent-height increment records), with an English data dictionary. Supplementary Data S3 provides the complete roughness sensitivity results as a CSV file. Supplementary Figure S16 compares ERA5 and WRF 10 m winds for the four selected periods, with the corresponding native-grid fields in Supplementary Data S4.

Author Contributions: J.Q. performed the simulations, processed and analyzed the data, prepared the figures and wrote the initial draft. Y.X. supervised the research, contributed to the study design, and reviewed and revised the manuscript. All authors have read and agreed to the published version of the manuscript.

Funding: The authors received no specific funding for this study.

Institutional Review Board Statement: Not applicable.

Informed Consent Statement: Not applicable.

Data Availability Statement: ERA5 data are available through the Copernicus Climate Data Store, and station observations are available from the NOAA/NCEI Integrated Surface Database. The complete namelist.wps and namelist.input files, analysis mask, selected-date list, station–model pairs, source data for the 20 heights and reproduction scripts are retained by the authors. Processed statistical data and analysis scripts are available from the corresponding author on reasonable request. Supplementary Data S1 contains all 2880 mean-wind records for the grid cells and heights within R1–R4, including traceable cropped-grid and d02 mass-grid indices. Supplementary Data S2 contains 76 records of domain-wide wind-speed increments across 19 adjacent-height intervals and four representative periods. All figures were generated deterministically from these data using Python 3.14.0 and Matplotlib 3.10.7. The large original WRF output files are available on reasonable request. Supplementary Data S3 reports the roughness sensitivity test. Supplementary Data S4 provides the native-grid period-mean 10 m wind fields used in the ERA5–WRF spatial comparison.

Conflicts of Interest: The authors declare no conflicts of interest.

References

1. Roney, J.A.; White, B.R. Definition and measurement of dust aeolian thresholds. *J. Geophys. Res. Earth Surf.* **2004**, *109*, F01013. https://doi.org/10.1029/2003JF000061.
2. Shao, Y.; Lu, H. A simple expression for wind erosion threshold friction velocity. *J. Geophys. Res. Atmos.* **2000**, *105*, 22437–22443. https://doi.org/10.1029/2000JD900304.
3. Blackadar, A.K. Boundary layer wind maxima and their significance for the growth of nocturnal inversions. *Bull. Am. Meteorol. Soc.* **1957**, *38*, 283–290. https://doi.org/10.1175/1520-0477-38.5.283.
4. Fiedler, S.; Schepanski, K.; Heinold, B.; Knippertz, P.; Tegen, I. Climatology of nocturnal low-level jets over North Africa and implications for modeling mineral dust emission. *J. Geophys. Res. Atmos.* **2013**, *118*, 6100–6121. https://doi.org/10.1002/jgrd.50394.
5. Heinold, B.; Knippertz, P.; Marsham, J.H.; Fiedler, S.; Dixon, N.S.; Schepanski, K.; Laurent, B.; Tegen, I. The role of deep convection and nocturnal low-level jets for dust emission in summertime West Africa: Estimates from convection-permitting simulations. *J. Geophys. Res. Atmos.* **2013**, *118*, 4385–4400. https://doi.org/10.1002/jgrd.50402.
6. Dong, Z.; Qu, J.; Lu, Q.; Qian, G. A discussion on feathery aeolian geomorphology in the Kumtagh Desert. *J. Desert Res.* **2008**, *28*, 1005–1010, 1214. (In Chinese)
7. E, Y.; Wang, J.; Yan, P.; Gao, S.; Wang, X.; Su, Z.; Liao, K.; Liu, H.; Ding, F. Evolution of palaeo-drainage system and its relationship with the formation of desert landform in the Kumtag Desert. *Acta Geogr. Sin.* **2008**, *63*, 725–734. Available online: https://www.geog.com.cn/EN/10.11821/xb200807006 (accessed on 20 November 2026). (In Chinese)
8. Zeng, S.L.; Gong, C.S.; Shang, K.Z.; Zeng, X.; Wang, S. Spatial and temporal variation of wind field in the Kumtagh Desert. *J. Desert Res.* **2011**, *31*, 28–33. (In Chinese)

9. Lü, P.; Narteau, C.; Dong, Z.; Rozier, O.; Courrech du Pont, S. Unravelling raked linear dunes to explain the coexistence of bedforms in complex dunefields. *Nat. Commun.* **2017**, *8*, 14239. https://doi.org/10.1038/ncomms14239.
10. Qian, G.; Yang, Z.; Xing, X.; Dong, Z.; Guo, Y. Seasonal morphological evolution and migration of granule ripples in the Sanlongsha Dune Field, northern Kumtagh Sand Sea, China. *Geomorphology* **2024**, *444*, 108951. https://doi.org/10.1016/j.geomorph.2023.108951.
11. Fu, G.; He, Q.; Wang, Y.; Ma, M.; Yin, L.; Zhang, Q. Characteristics of wind, temperature, humidity profiles and energy exchange in the surface layer in the southern edge of Taklimakan Desert. *Arid. Land Geogr.* **2024**, *47*, 68–80. Available online: https://www.geores.com.cn/ghqdl/CN/10.12118/j.issn.1000%EF%BC%8D6060.2023.445 (accessed on 20 November 2026). (In Chinese)
12. Liu, X.; Kang, Y.; Chen, H.; Lu, H. Comparison of surface wind speed and wind speed profiles in the Taklimakan Desert. *PeerJ* **2022**, *10*, e13001. https://doi.org/10.7717/peerj.13001.
13. Ge, J.M.; Liu, H.; Huang, J.; Fu, Q. Taklimakan Desert nocturnal low-level jet: Climatology and dust activity. *Atmos. Chem. Phys.* **2016**, *16*, 7773–7783. https://doi.org/10.5194/acp-16-7773-2016.
14. Su, L.; Lu, C.; Yuan, J.; Wang, X.; He, Q.; Xia, H. Measurement report: The promotion of the low-level jet and thermal effects on the development of the deep convective boundary layer at the southern edge of the Taklimakan Desert. *Atmos. Chem. Phys.* **2024**, *24*, 10947–10963. https://doi.org/10.5194/acp-24-10947-2024.
15. Gadal, C.; Delorme, P.; Narteau, C.; Wiggs, G.F.S.; Baddock, M.; Nield, J.M.; Claudin, P. Local wind regime induced by giant linear dunes: Comparison of ERA5-Land reanalysis with surface measurements. *Bound.-Layer Meteorol.* **2022**, *185*, 309–332. https://doi.org/10.1007/s10546-022-00733-6.
16. Clements, M.; Washington, R. Atmospheric controls on mineral dust emission from the Etosha Pan, Namibia: Observations from the CLARIFY-2016 field campaign. *J. Geophys. Res. Atmos.* **2021**, *126*, e2021JD034746. https://doi.org/10.1029/2021JD034746.
17. Hersbach, H.; Bell, B.; Berrisford, P.; Hirahara, S.; Horányi, A.; Muñoz-Sabater, J.; Nicolas, J.; Peubey, C.; Radu, R.; Schepers, D.; et al. The ERA5 global reanalysis. *Q. J. R. Meteorol. Soc.* **2020**, *146*, 1999–2049. https://doi.org/10.1002/qj.3803.
18. Skamarock, W.C.; Klemp, J.B.; Dudhia, J.; Gill, D.O.; Liu, Z.; Berner, J.; Wang, W.; Powers, J.G.; Duda, M.G.; Barker, D.M.; et al. *A Description of the Advanced Research WRF Model Version 4*; NCAR Technical Note NCAR/TN-556+STR; National Center for Atmospheric Research: Boulder, CO, USA, 2019. https://doi.org/10.5065/1dfh-6p97.
19. Wang, M.; Xu, X.; Xu, H.; Lenschow, D.H.; Zhou, M.; Zhang, J.; Wang, Y. Features of the deep atmospheric boundary layer over the Taklimakan Desert in the summertime and its influence on regional circulation. *J. Geophys. Res. Atmos.* **2019**, *124*, 12755–12772. https://doi.org/10.1029/2019JD030714.
20. Xu, X.; Li, X.; Zhang, Y.; Gao, Z.; Sun, J. Application of WRF-LES on the Simulation of Seasonal Characteristics of Atmospheric Boundary Layer Structure in Taklamakan Desert. *Remote Sens.* **2024**, *16*, 558. https://doi.org/10.3390/rs16030558.
21. Han, Z.; Ge, J.; Chen, X.; Hu, X.; Yang, X.; Du, J. Dust activities induced by nocturnal low-level jet over the Taklimakan Desert from WRF-Chem simulation. *J. Geophys. Res. Atmos.* **2022**, *127*, e2021JD036114. https://doi.org/10.1029/2021JD036114.
22. Han, Z.; Gao, M.; Zhang, H.; Sun, X.; Wu, B. Impact of seasonal diurnal variation characteristics of low-level jet on wind energy utilization in Taklimakan Desert. *Water Resour. Hydropower Eng.* **2025**, *56*, 740–748.. https://doi.org/10.13928/j.cnki.wrahe.2025.S2.113. (In Chinese)
23. Solbakken, K.; Birkelund, Y.; Samuelsen, E.M. Evaluation of surface wind using WRF in complex terrain: Atmospheric input data and grid spacing. *Environ. Model. Softw.* **2021**, *145*, 105182. https://doi.org/10.1016/j.envsoft.2021.105182.
24. Al Oqaily, D.; Giani, P.; Crippa, P. Evaluating WRF Multiscale Wind Simulations in Complex Terrain: Insights From the Perdigão Field Campaign. *J. Geophys. Res. Atmos.* **2025**, *130*, e2025JD044055. https://doi.org/10.1029/2025JD044055.
25. Ma, Y. Near-surface wind profiles from numerical model predictions. Part I: Algorithms and comparisons with wind profile based on Monin–Obukhov similarity theory. *Q. J. R. Meteorol. Soc.* **2024**, *150*, 3875–3890. https://doi.org/10.1002/qj.4779.
26. Jin, B.; Zhang, Y.; Hasi, E.; Su, Z.; Kong, D.; Yu, J.; Cheng, L.; Fei, B.; Han, X.; Zhang, Y.; et al. Chromatic characteristics of sediments in the northern Kumtagh Desert and analysis of alternating light and dark landscapes on dune surfaces. *Acta Geogr. Sin.* **2024**, *79*, 2297–2311. (In Chinese) https://doi.org/10.11821/dlxb202409009.
27. National Centers for Environmental Information (NCEI). Global Hourly—Integrated Surface Database (ISD). NOAA/NCEI. Available online: https://www.ncei.noaa.gov/products/land-based-station/integrated-surface-database (accessed on 24 August 2026).
28. Pleim, J.E. A combined local and nonlocal closure model for the atmospheric boundary layer. Part I: Model description and testing. *J. Appl. Meteorol. Climatol.* **2007**, *46*, 1383–1395. https://doi.org/10.1175/JAM2539.1.

29. Chen, F.; Dudhia, J. Coupling an advanced land surface-hydrology model with the Penn State-NCAR MM5 modeling system. Part I: Model implementation and sensitivity. *Mon. Weather Rev.* **2001**, *129*, 569–585. https://doi.org/10.1175/1520-0493(2001)129<0569:CAALSH>2.0.CO;2.
30. Iacono, M.J.; Delamere, J.S.; Mlawer, E.J.; Shephard, M.W.; Clough, S.A.; Collins, W.D. Radiative forcing by long-lived greenhouse gases: Calculations with the AER radiative transfer models. *J. Geophys. Res. Atmos.* **2008**, *113*, D13103. https://doi.org/10.1029/2008JD009944.
31. Hong, S.Y.; Lim, J.O.J. The WRF Single-Moment 6-Class Microphysics Scheme (WSM6). *J. Korean Meteorol. Soc.* **2006**, *42*, 129–151.
32. Kain, J.S. The Kain-Fritsch convective parameterization: An update. *J. Appl. Meteorol.* **2004**, *43*, 170–181. https://doi.org/10.1175/1520-0450(2004)043<0170:TKCPAU>2.0.CO;2.
33. Wang, Y.; Sayit, H.; Mamtimin, A.; Zhu, J.; Zhou, C.; Huo, W.; Yang, F.; Yang, X.; Gao, J.; Zhao, X. Evaluation of five planetary boundary layer schemes in WRF over China's largest semi-fixed desert. *Atmos. Res.* **2021**, *256*, 105567. https://doi.org/10.1016/j.atmosres.2021.105567.
34. Li, M.; Zhang, Z.; Ju, C.; Li, H. Sensitivity of temperature and precipitation characteristics to land use classification over the Taklimakan Desert and surrounding area. *Theor. Appl. Climatol.* **2023**, *154*, 987–998. https://doi.org/10.1007/s00704-023-04608-9.
35. Ranjbar Saadatabadi, A.; Hossein Hamzeh, N.; Kaskaoutis, D.G.; Ghasabi, Z.; Penchah, M.M.; Sotiropoulou, R.-E.P.; Habibi, M. Optimization and Evaluation of the Weather Research and Forecasting (WRF) Model for Wind Energy Resource Assessment and Mapping in Iran. *Appl. Sci.* **2024**, *14*, 3304. https://doi.org/10.3390/app14083304.
36. Wilks, D.S. *Statistical Methods in the Atmospheric Sciences*, 4th ed.; Elsevier: Amsterdam, The Netherlands, 2019.
37. Liu, N.; Peng, H.; Zhang, L.; Zhang, L.; Wu, D. The triple-benefit potential of desert wind farms in China: Energy, resource complementarity, and climate effect. *Earth's Future* **2026**, *14*, e2026EF008179. https://doi.org/10.1029/2026EF008179.
38. Hahmann, A.N.; Sīle, T.; Witha, B.; Davis, N.N.; Dörenkämper, M.; Ezber, Y.; García-Bustamante, E.; González-Rouco, J.F.; Navarro, J.; Olsen, B.T.; et al. The making of the New European Wind Atlas—Part 1: Model sensitivity. *Geosci. Model Dev.* **2020**, *13*, 5053–5078. https://doi.org/10.5194/gmd-13-5053-2020.
39. Hasager, C.B.; Hahmann, A.N.; Ahsbahs, T.; Karagali, I.; Sile, T.; Badger, M.; Mann, J. Europe's offshore winds assessed with synthetic aperture radar, ASCAT and WRF. *Wind Energy Sci.* **2020**, *5*, 375–390. https://doi.org/10.5194/wes-5-375-2020.
40. Dörenkämper, M.; Olsen, B.T.; Witha, B.; Hahmann, A.N.; Davis, N.N.; Barcons, J.; Ezber, Y.; García-Bustamante, E.; González-Rouco, J.F.; Navarro, J.; et al. The Making of the New European Wind Atlas—Part 2: Production and evaluation. *Geosci. Model Dev.* **2020**, *13*, 5079–5102. https://doi.org/10.5194/gmd-13-5079-2020.
41. Lin, D.; Khan, B.; Katurji, M.; Bird, L.; Faria, R.; Revell, L.E. WRF4PALM v1.0:a mesoscale dynamical driver for the microscale PALM model system 6.0. *Geosci. Model Dev.* **2021**, *14*, 2503–2524. https://doi.org/10.5194/gmd-14-2503-2021.
42. World Meteorological Organization (WMO). *Guide to Climatological Practices*, 2018 ed.; WMO-No.100; World Meteorological Organization: Geneva, Switzerland, 2018.
43. Shao, Y.; Mikami, M. Heterogeneous saltation: Theory, observation and comparison. *Bound.-Layer Meteorol.* **2005**, *115*, 359–379. https://doi.org/10.1007/s10546-004-7089-2.
44. Kimura, R.; Shinoda, M. Spatial distribution of threshold wind speeds for dust outbreaks in northeast Asia. *Geomorphology* **2010**, *114*, 319–325. https://doi.org/10.1016/j.geomorph.2009.07.014.
45. Laurent, B.; Marticorena, B.; Bergametti, G.; Chazette, P.; Maignan, F.; Schmechtig, C. Simulation of the mineral dust emission frequencies from desert areas of China and Mongolia using an aerodynamic roughness length map derived from the POLDER/ADEOS 1 surface products. *J. Geophys. Res. Atmos.* **2005**, *110*, D18S04. https://doi.org/10.1029/2004JD005013.
46. Zhang, Q.; Cao, X.; Wei, G.; Huang, R. Observation and study of land surface parameters over Gobi in typical arid region. *Adv. Atmos. Sci.* **2002**, *19*, 121–135. https://doi.org/10.1007/s00376-002-0039-3.
47. Foken, T. 50 years of the Monin-Obukhov similarity theory. *Bound.-Layer Meteorol.* **2006**, *119*, 431–447. https://doi.org/10.1007/s10546-006-9048-6.
48. Yang, B.; Finn, D.; Rich, J.; Gao, Z.; Liu, H. Effects of Low-Level Jets on Near-Surface Turbulence and Wind Direction Changes in the Nocturnal Boundary Layer. *J. Geophys. Res. Atmos.* **2023**, *128*, e2022JD037657. https://doi.org/10.1029/2022JD037657.
49. Tuononen, M.; O'Connor, E.J.; Sinclair, V.A.; Vakkari, V. Low-level jets over Utö, Finland, based on Doppler lidar observations. *J. Appl. Meteorol. Climatol.* **2017**, *56*, 2577–2594. https://doi.org/10.1175/JAMC-D-16-0411.1.
50. Langot, F.; Crevoisier, C.; Lauvaux, T.; Abdallah, C.; Pernin, J.; Lin, X.; Saunois, M.; Guedj, A.; Ponthieu, T.; Moyé, J.; et al. Evaluating Weather and Chemical Transport Models at High Latitudes using MAGIC2021 Airborne Measurements. *Atmos. Meas. Tech.* **2025**, *18*, 5955–5983. https://doi.org/10.5194/amt-18-5955-2025.

51. Cheynet, E.; Diezel, J.M.; Haakenstad, H.; Breivik, Ø.; Peña, A.; Reuder, J. Tall wind profile validation of ERA5, NORA3, and NEWA datasets using lidar observations. *Wind Energy Sci.* **2025**, *10*, 733–754. https://doi.org/10.5194/wes-10-733-2025.
52. Louge, M.Y.; Valance, A.; Fang, J.; Harnett, S.J.; Porté-Agel, F.; Chasle, P. Evolution of Turbulent Boundary Conditions on the Surface of Large Barchan Dunes: Anomalies in Aerodynamic Roughness and Shear Velocity, Aeolian Threshold, and the Role of Dune Skewness. *J. Geophys. Res. Earth Surf.* **2024**, *129*, e2023JF007599. https://doi.org/10.1029/2023JF007599.
53. Zhang, Q.; Huang, R.H.; Tian, H. A parameterization scheme of surface turbulent momentum and sensible heat over the Gobi underlying surface. *Adv. Atmos. Sci.* **2003**, *20*, 111–118. https://doi.org/10.1007/BF03342055.
54. Gryning, S.E.; Batchvarova, E.; Brümmer, B.; Jørgensen, H.; Larsen, S. On the extension of the wind profile over homogeneous terrain beyond the surface boundary layer. *Bound.-Layer Meteorol.* **2007**, *124*, 251–268. https://doi.org/10.1007/s10546-007-9166-9.
55. Fécan, F.; Marticorena, B.; Bergametti, G. Parametrization of the increase of the aeolian erosion threshold wind friction velocity due to soil moisture for arid and semi-arid areas. *Ann. Geophys.* **1999**, *17*, 149–157. https://doi.org/10.1007/s00585-999-0149-7.
56. Sharratt, B.S.; Vaddella, V. Threshold friction velocity of crusted windblown soils in the Columbia Plateau. *Aeolian Res.* **2014**, *15*, 227–234. https://doi.org/10.1016/j.aeolia.2014.08.002.
57. Dong, H.; Zhang, Y.; Tao, T.; Du, X.; Zou, Y.; Cao, S. Sensitivity of near-ground wind to PBL schemes, reanalysis data, and nudging in month-long WRF simulations in the Tibetan Plateau with highly complex terrain. *Atmos. Res.* **2025**, *323*, 108161. https://doi.org/10.1016/j.atmosres.2025.108161.

Disclaimer/Publisher's Note: The statements, opinions and data contained in all publications are solely those of the individual author(s) and contributor(s) and not of MDPI and/or the editor(s). MDPI and/or the editor(s) disclaim responsibility for any injury to people or property resulting from any ideas, methods, instructions or products referred to in the content.